Precambrian Research 235 (2013) 20–35

Contents lists available at ScienceDirect

Precambrian Research

journal homepage: www.elsevier.com/locate/precamres

Terminal Proterozoic cyanobacterial blooms and phosphogenesis documented by the Doushantuo granular phosphorites I: *In situ* micro-analysis of textures and composition

Zhenbing She[a,b,*], Paul Strother[c], Gregory McMahon[d], Larry R. Nittler[e], Jianhua Wang[e], Jianhua Zhang[f], Longkang Sang[a], Changqian Ma[a,b], Dominic Papineau[c,g]

[a] *State Key Laboratory of Geological Processes and Mineral Resources, Wuhan 430074, China*
[b] *Faculty of Earth Sciences, China University of Geosciences, Wuhan 430074, China*
[c] *Department of Earth and Environmental Sciences, Boston College, Chestnut Hill, MA 02467, USA*
[d] *Nanofabrication Cleanroom Facility, Boston College, Newton, MA 02459, USA*
[e] *Department of Terrestrial Magnetism, Carnegie Institution of Washington, Washington, DC 20015, USA*
[f] *Mine Planning and Designing Institute of Yilin District, Yichang 443100, China*
[g] *Geophysical Laboratory, Carnegie Institution of Washington, Washington, DC 20015, USA*

ARTICLE INFO

Article history:
Received 19 December 2012
Received in revised form 17 May 2013
Accepted 20 May 2013
Available online 13 June 2013

Keywords:
Doushantuo
Granular phosphorites
Extracellular polymeric substances
Accretionary growth
Cyanobacteria
Phosphatization

ABSTRACT

In order to ascertain the origin of granular phosphorites and the roles of microorganisms in phosphogenesis, we conducted comprehensive petrographic surveys and correlated *in situ* micro-analyses of granular phosphorites from the Doushantuo Formation near Yichang, South China. Phosphatic granules display organically-zoned internal structures often associated with abundant cyanobacteria-like microfossils. The internal ultrastructure of the granules, as documented by Raman microspectroscopy, scanning electron microscopy (SEM) and transmission electron microscopy (TEM), is characterized by randomly-oriented apatite nano-crystals embedded with ubiquitous carbonaceous particles in the apatite groundmass. These represent primary textures formed by the rapid growth of apatite provided with abundant nucleation sites within microbial biofabrics. NanoSIMS elemental mapping revealed close correspondence of carbon and nitrogen with microfossil structures at the cellular and sub-cellular level. We propose that the Doushantuo granules themselves were formed by microbially-mediated accretionary growth followed by rapid phosphatization occurring at the sediment–water interface. Extracellular polymeric substances (EPS) produced by cyanobacteria would have played crucial roles in these processes by promoting aggregated granule growth in addition to providing nucleation sites for apatite crystallization. While previous studies have suggested a dominant role of sulfur-metabolizing microorganisms in the precipitation of phosphate in phosphorites, new observations indicate that the emplacement of most sulfur-bearing minerals in the Doushantuo phosphorites postdate phosphatization itself. Our new model of phosphorite formation thus places cyanobacterial EPS as an earlier key component of the mineralization of the Doushantuo granular phosphorites.

1. Introduction

Phosphorus usually occurs as a minor or trace constituent in igneous, metamorphic and sedimentary rocks but can be enriched in marine sedimentary phosphorites composed of carbonate fluorapatite. Although formation of sedimentary phosphate deposits is largely a Phanerozoic phenomenon (Cook, 1992), worldwide phosphogenesis, representing periods of accelerated activity in global phosphorus cycles, has occurred at the end of the Paleoproterozoic and of the Neoproterozoic (Papineau, 2010). Phosphorus plays a vital role in governing primary productivity in the biosphere, thereby interacting with other biogeochemical cycles which, in turn, help regulate Earth's climate (Föllmi, 1996).

Models of the phosphorus cycle are largely constructed on the basis of observations of modern or recent phosphogenic environments such as the coastal upwelling regions of Namibia, Chile and Peru (Arning et al., 2009; *e.g.*, Föllmi, 1996). Phosphogenesis within these upwelling environments occurs when pore-water becomes supersaturated with dissolved phosphate (Burnett, 1977; Föllmi, 1996). The immediate source of sedimentary phosphate is considered to be released from organic matter which is degraded

* Corresponding author at: Faculty of Earth Sciences, China University of Geosciences, Wuhan 430074, China. Tel.: +86 27 67883001.
E-mail address: zbsher@gmail.com (Z. She).

0301-9268/$ – see front matter © 2013 Elsevier B.V. All rights reserved.
http://dx.doi.org/10.1016/j.precamres.2013.05.011

by microbially-mediated redox reactions, although phosphate is ultimately mainly derived from weathering of continental crust (Föllmi, 1996). In non-upwelling environments, however, the concentration of phosphorus near the water-sediment interface is believed to occur by Fe-redox pumping where Fe-oxyhydroxides transport phosphate from the oxic water column to the suboxic/anoxic seafloor (Heggie et al., 1990; Nelson et al., 2010). This model requires a redox-stratified water column which is thought to be characteristic of Proterozoic oceans (Anbar and Knoll, 2002). Alternatively, clay minerals, particularly illite, have been proposed to have the potential to adsorb phosphate and thereby concentrate phosphorus in interstitial fluids (Bremner, 1980). Although these models may partly explain the delivery and enrichment of phosphate at the bottom of the water column or in pore water solutions, they do not address how calcium phosphate eventually precipitates to form phosphorites.

Most ancient phosphorites, especially Precambrian phosphorites, retain a granular sedimentary fabric (Nelson et al., 2010; Soudry and Southgate, 1989; Ye et al., 1989; Zhao, 1985). The origin of phosphate granules is generally attributed to reworking of pre-existing phosphatic sediments. Although some granular phosphorites exhibit some features indicating formation in agitated, environments above wave base, a number of features are not easily explained merely by reworking. These include the frequently observed co-occurrence of "high-energy oöids" and "low-energy-indicating" mud matrix (Dahanayake and Krumbein, 1986; Horton et al., 1980; Riggs, 1979) along with evidence for *in situ* formation (Soudry and Southgate, 1989). It is clear that the underlying mechanisms in the formation of granular phosphorites requires more investigation.

In this work, we examined the petrography of a suite of granular phosphorites collected from the Doushantuo Formation in Yichang, South China. Microfossiliferous samples were selected for further *in situ* micro-analyses of petrographic fabrics, mineral structure and geochemistry. Our new data shed light on the underlying diagenetic processes of granular phosphorite formation and on the crucial roles of cyanobacterial EPS in granule formation and phosphate precipitation. This, in turn, allows us to propose a new biogeochemical model for phosphogenesis that addresses the formation of the Doushantuo granular phosphorites and might be applicable to other marine phosphorites.

2. Geological setting and samples

The Doushantuo Fm is a carbonate-black shale-phosphorite sequence that is widespread in South China with patchy outcrops covering the entire Yangtze Block for more than 1,620,000 km^2 (Jiang et al., 2011). It is underlain by diamictites of the Nantuo Fm, which represents the sedimentary record equivalent to the Marinoan snowball Earth glaciation, and is overlain by carbonates of the Dengying Fm. The Doushantuo Fm is important because it contains exceptionally well-preserved fossil evidence for putative earliest animal embryos (*e.g.*, Xiao et al., 1998). It is also economically important because of the discovery of major phosphate deposits that account for 51% of the total phosphorus reserves in China according to an early estimate (Ye et al., 1989). Paleogeographic reconstructions show that the vast proportion of the Doushantuo Fm in the Yangtze platform was deposited on a rimmed carbonate shelf with a shelf margin-shoal complex that restricted the shelf lagoon from the open ocean (Fig. 1a). The distribution of phosphate deposits in South China does not correspond to the general paleogeographic regime, but rather are controlled by local uplifts and depressions (Ye et al., 1989).

Although there are considerable lateral variations in stratigraphic thickness (from 40 m to 300 m), the Doushantuo Fm is generally described in terms of four lithologically-defined members (Fig. 1c). Regional stratigraphic correlations are made on the basis of two distinctive marker beds, the cap carbonate at the base (mem. I) and the organic-rich black shale at the top of the formation (mem. IV) (Jiang et al., 2011; McFadden et al., 2008; Zhu et al., 2007). Zircon U–Pb TIMS ages of three ash layers were obtained from the Yangtze Gorges area (Condon et al., 2005), one within the cap carbonate itself (635.2 ± 0.6 Ma), another 9 m above (632.5 ± 0.5 Ma), and the third just below the Doushantuo/Dengying boundary (551.1 ± 0.7 Ma). SHRIMP U–Pb dating of zircons from another ash layer in mem. II in the Zhangcunping section 65 km north of Yichang City yielded an age of 614.0 ± 7.6 Ma (Liu et al., 2009). Two Re-Os ages of 598 ± 16 Ma (Kendall et al., 2009) and 593 ± 17 Ma (Zhu et al., 2013) have been reported from black shale of Member IV at Jiulongwan. Collectively, these data place the Doushantuo Formation entirely within the Ediacaran Period and specifically between 635 and 542 Ma.

We focus on the lower part of mem. II of the Doushantuo Fm in the Taopinghe phosphorus mine (GPS coordinates: 31°16′29.9″N, 111°16′30.8″E), ~65 km north of Yichang, which contains major phosphate deposits (Fig. 1b). As is shown in Fig. 1c, the phosphorus-bearing sequence begins with repeated shale-phosphorite cycles and evolves upward into phosphorites with minor dolostones and eventually into thick-bedded dolostones without phosphorite. Among the three main phosphorus-bearing horizons ($Ph1^1$, $Ph1^2$ and $Ph1^3$, Fig. 1c), only the upper one ($Ph1^3$), which is around 6 meters thick and contains P_2O_5 up to 35 wt%, is currently under mining. The samples studied here were mainly collected from outcrops and mining tunnels of $Ph1^3$ in the Taopinghe mining area.

3. Methods

3.1. Optical microscopy

Petrographic studies were performed on polished thin sections with an Olympus BX51 petrographic microscope fitted with dry 4×, 10×, 40×, and 100× long working-distance objectives. The images obtained with the microscope were captured with an Olympus UC50 CCD camera.

3.2. Raman microspectroscopy

Confocal laser Raman microspectroscopy was performed at Boston College using a WiTec alpha 300 R system equipped with a 532 nm laser with output power maintained at ~5 mW. Raman hyperspectral scans were performed under a 100 × objective (N.A. = 0.9) with a 50 μm diameter optic fiber and collected on a Peltier-cooled EMCCD detector. Spatial resolution was ~360 nm/pixel and spectral resolution was ~4 cm^{-1}. Individual spectra shown in this work represent averages of selected regions with similar spectral characteristics. Hyperspectral images were generated by mapping peak intensity from spectral datasets and include information on both chemical composition and textures (Bernard et al., 2008). The analyses were performed at least 0.5μ below the thin section surface, therefore ruling out potential artifacts induced by polishing or surface contamination (Papineau et al., 2010; Pasteris, 1989).

3.3. Scanning electron microscopy

Scanning electron microscopy (SEM) was carried out at the class 1000 cleanroom at Boston College using a JEOL JSM7001F field-emission SEM equipped with an energy dispersive X-ray spectrometer (EDS) and back-scattered electron (BSE) detector. Accelerating voltage was 2.5 kV for SEI mode and 7.5 kV for BSE mode during imaging and EDS analysis. Freshly broken chips of

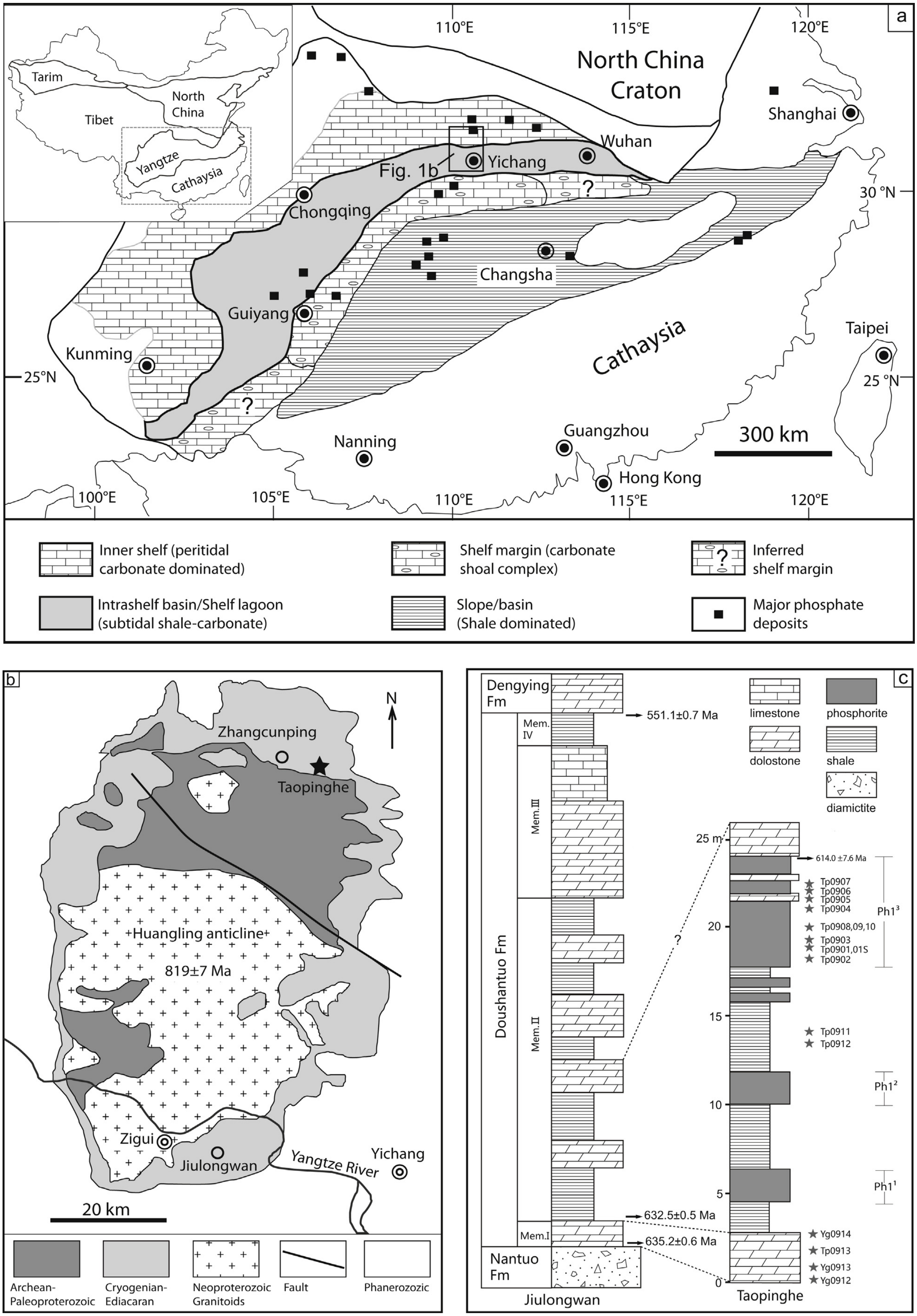
a
110°E
115°E
120°E
North China Craton
Tarim
North China
Tibet
Yangtze
Cathaysia
Shanghai
Wuhan
Yichang
Fig. 1b
?
30 °N
Chongqing
Changsha
Guiyang
Kunming
Cathaysia
Taipei
25°N
25 °N
Nanning
Guangzhou
Hong Kong
300 km
100°E
105°E
110°E
115°E
120°E
Inner shelf (peritidal carbonate dominated)
Shelf margin (carbonate shoal complex)
Inferred shelf margin
Intrashelf basin/Shelf lagoon (subtidal shale-carbonate)
Slope/basin (Shale dominated)
Major phosphate deposits
b
N
Zhangcunping
Taopinghe
Huangling anticline
819±7 Ma
Zigui
Jiulongwan
Yangtze River
Yichang
20 km
Archean-Paleoproterozoic
Cryogenian-Ediacaran
Neoproterozoic Granitoids
Fault
Phanerozoic
c
Dengying Fm
Doushantuo Fm
Mem. IV
Mem.III
Mem.II
Mem.I
Nantuo Fm
551.1±0.7 Ma
632.5±0.5 Ma
635.2±0.6 Ma
Jiulongwan
limestone
phosphorite
dolostone
shale
diamictite
25 m
20
15
10
5
0
614.0 ±7.6 Ma
Tp0907
Tp0906
Tp0905
Tp0904
Tp0908,09,10
Tp0903
Tp0901,01S
Tp0902
Ph1³
Tp0911
Tp0912
Ph1²
Ph1¹
Yg0914
Tp0913
Yg0913
Yg0912
Taopinghe

samples were cleaned with ultrasonication, rinsed with DI water, and dried in air. Samples were analyzed without surface coating.

3.4. Focused ion beam milling and lift-out

Focused ion beam (FIB) milling and lift-out were performed with a JEOL JIB 4500 MultiBeam system in the class 1000 clean-room for microfabrication at Boston College. Targets 3–7 μm below the surface of thin sections were thoroughly characterized by transmitted light microscopy and Raman microspectroscopy and located by SEM imaging. A 15 × 1 μm protective tungsten shield was deposited using $W(CO)_6$ gas exposed to the Ga^+ beam on the surface of the gold-coated target prior to milling. A focused 30 keV Ga^+ primary beam was then used to sputter away material from both sides of the deposited tungsten mask, leaving a ∼1 μm thick vertical section approximately 12 × 12 μm in size. The bottom and sides of the section were then cut by the Ga^+ beam, leaving only small parts on the top of both sides connected to the thin section. A tungsten micro-needle controlled by a Kleindiek Nanotechnik micromanipulator system, was moved toward the sample, welded with W onto the FIB foil using $W(CO)_6$. The remaining tabs on the section were cut, freeing the membrane from the sample matrix. The micromanipulator was then used to move the foil to a Cu TEM half grid, where the foil was finally welded with W and the connection with the needle cut. Final thinning was done by sputtering on both sides of the section to achieve a thickness of 100–150 nm. During this phase, care was taken to progressively reduce the Ga^+ beam current from 5 nA to less than 50 pA, which yields FIB foils with uniform surfaces (Wirth, 2009; Zega et al., 2007) and with minimal Ga^+ implantation in the foil. The last thinning step was specifically performed during a new session, before which *a* > 15 min oxygen plasma cleaning, with an XEI Scientific Evactron system, minimized the amount of organic volatiles in the sample chamber.

3.5. Transmission electron microscopy

The FIB foil (TP0901S_09) was analyzed using a JEOL-2010F transmission electron microscope (TEM) operating at a voltage potential of 200 keV in the physics department at Boston College. High-resolution TEM imaging was used to visualize the morphology of nanoscale apatite crystals and organic matter and their spatial relationships within possible microfossils. Mineral compositions were determined spot by spot with an lN2-cooled EDS detector attached to the sample chamber. The Cu half-grid was inserted directly into the TEM without a conductive coating.

3.6. NanoSIMS elemental mapping

NanoSIMS studies were conducted on two FIB foils and a polished and carefully cleaned thin section of the phosphorite to document the biogenicity of the carbonaceous matter and their surrounding groundmass (Oehler et al., 2009, 2010). Prior to analysis, the thin section was repolished using 0.3 μm cerium oxide in D.I. water to minimize surface contamination by organic matter and then repeatedly rinsed with D.I. water. Elemental maps were obtained with the Cameca NanoSIMS 50 L ion microprobe at the Carnegie Institution of Washington. Analyses were performed with a 16 kV, 2 pA, ∼150 nm $^{137}Cs^+$ primary beam under ultra-high vacuum between 2×10^{-9} and 2×10^{-10} torr. The instrument was tuned for a mass resolving power sufficient to resolve $^{12}C^1H^-$ from $^{13}C^-$ and $^{12}C^{14}N^-$ from $^{13}C_2{}^-$.

Elemental maps were generated with the NanoSIMS by rastering the beam on the sample with simultaneous detection of negative secondary ions $^{12}C^-$, $^{12}C^1H^-$, $^{12}C^{14}N^-$, $^{16}O^-$, $^{31}P^-$ and $^{32}S^-$ on electron-multiplier detectors. Secondary ion counts relative to $^{12}C^-$ represent first-order estimates for comparisons of elemental abundance between different targets. These estimates are only semi-quantitative and only in terms of secondary ion counts because a suitable phosphorite standard with homogeneous H, O, N, P, and S abundances (needed to normalize actual atomic abundances of these elements) was unavailable. Therefore, we caution that estimates of relative secondary ion counts do not reflect actual atomic ratios because different atoms and molecules have different ionization efficiency during sputtering.

Prior to analysis, the samples were pre-sputtered on a slightly larger area than the imaging target for 10 cycles with a defocused primary beam (∼5 min at 100 pA for FIB foils and ∼10 min at 1 nA for targets in thin sections) to eliminate possible surface contaminants and to implant Cs^+ for enhanced negative secondary ion emission. Measurements of 50–60 cycles (15–35 min total) were conducted to ensure secondary ion beam stability and achieve stable count rates. Generally only the last 20 cycles, after the count rates were stable and had reached a plateau, were used for data analysis. Imaged areas were from 15 μm × 15 μm to 25 μm × 25 μm. Elemental maps of ^{12}C, $^{12}C^1H$, $^{12}C^{14}N$, ^{16}O, ^{31}P and ^{32}S were generated with the L'image software package (L.R. Nittler, Carnegie Institution of Washington).

4. Results

4.1. Texture and mineralogy

The Taopinghe phosphorites are mostly banded rocks and are characterized by repeated 2–10 mm-thick bands (Fig. 2a and b), representing sedimentary cycles. The dominant lithology is granular phosphorite composed of densely packed, sand-sized granules (Fig. 2c). Fine laminae or massive (homogeneous) layers are occasionally present in between granular bands (Fig. 2d). These non-granular layers are structureless or show faint, subparallel lamination, and rarely contain microfossils. Subangular to subrounded detrital quartz grains and rock fragments are locally present in some samples. In the upper part of the sequence, where phosphorite often occur along with dolostone, carbonatization of phosphate granules and cement is often observed (white matrix in Fig. 2b).

4.1.1. The granules

The granules are generally elliptical with variable sizes although elongated or irregular shapes are also present (Fig. 2c). Statistics of grain sizes of 450 granules from four thin sections yielded major axes ranging between 150 μm and 900 μm and minor axes from 100 μm to 700 μm, with most falling in the size range of medium sand. The granules are typically brownish and "dirty" and appear to be isotropic or cryptocrystalline (Fig. 2c).

A primary feature of the phosphatic granules is their oncoid-like zoning (Fig. 2c, e and f). Intra-granular zoning includes both asymmetric (Fig. 2e) and concentric patterns (Fig. 2f) typically displayed as two to five zones. Fig. 2e shows a granule that features asymmetrical non-isopachous zoning. Microfossils are observed in

Fig. 1. Geological maps and stratigraphic columns: (a) a proposed paleogeographic map of the Yangtze Block during the early Ediacaran Period (modified after Jiang et al., 2011), showing major phosphate deposits in the Doushantuo Formation (Ye et al., 1989). Inset shows major blocks in China, (b) simplified geological map of the study area. (c) Generalized stratigraphic column of the Doushantuo Formation in Jiulongwan (Xiao et al., 2012) and exposed section in Taopinghe showing sampled layers (this study). $Ph1^1$, $Ph1^2$ and $Ph1^3$ refer to the three major phosphorus-bearing beds in the Taopinghe mining area. Radiometric ages are from Condon et al. (2005) and Liu et al. (2009).

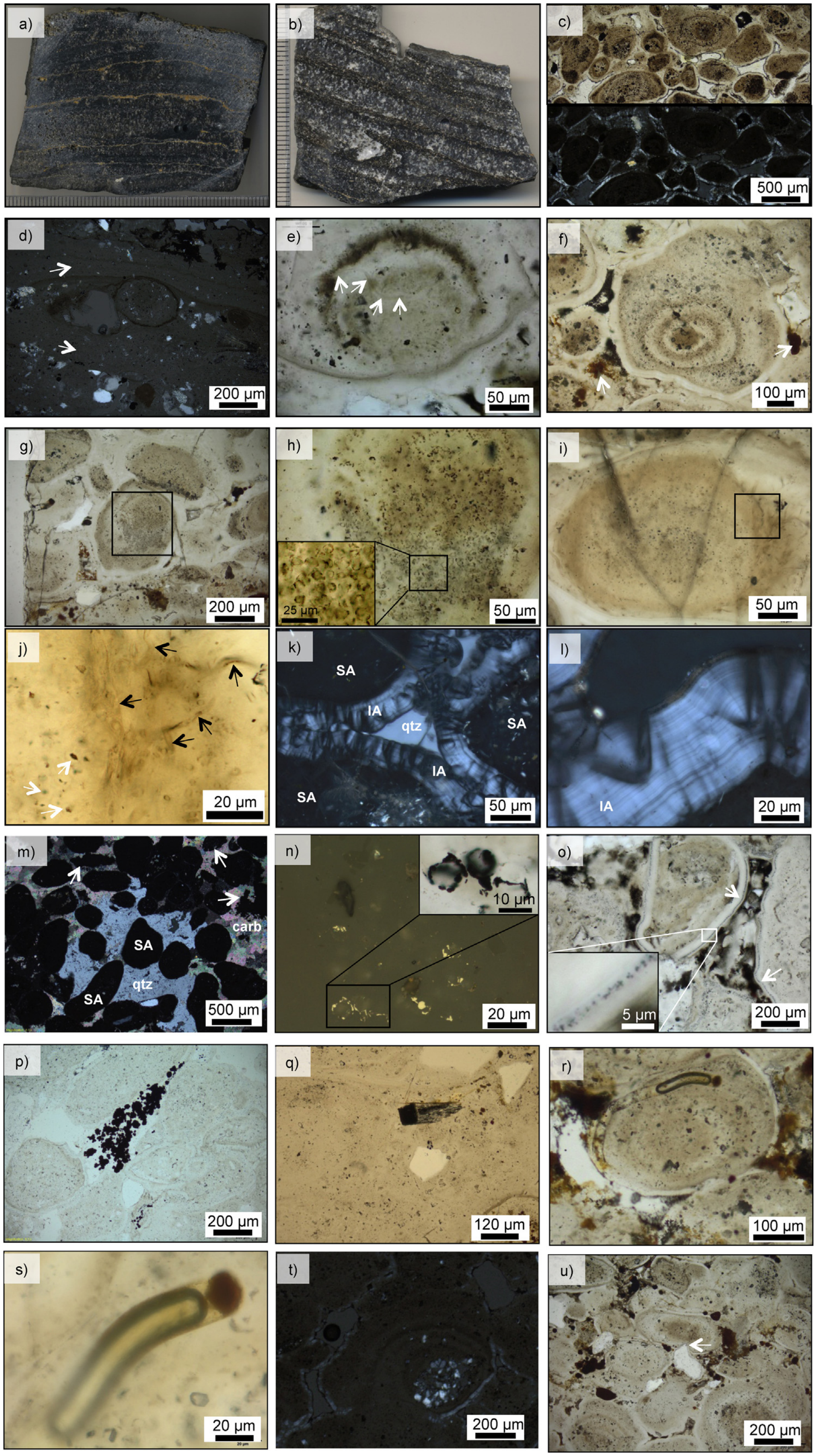

Fig. 2. Structures and microstructures of the Doushantuo phosphorites: (a) slab of phosphorite displaying banded structure bound by brownish yellow laminae, (b) banded phosphorite showing partial replacement by carbonate mineral (white patches), (c)–(u) photomicrographs of the phosphorites (transmitted light, plane polarized: (e)–(j), (o)–(s), (u) and the upper figure of (c); transmitted light, crossed nicols: (d), (k)–(m), (t) and the lower figure of (c); reflected light: (n)), (c) granular phosphorite showing concentric or asymmetric zoning and isotropic features, (d) local occurrence of non-granular layers (arrows) and detrital quartz and lithic fragments, (e) an asymmetrically-zoned granule, note the sinuous filament (arrows) crosscutting the zones, (f) a concentrically-zoned granule and interstitial hematites (arrows), (g) granule containing

almost every granule, including populations of coccoidal (Fig. 2g and h) and filamentous (Fig. 2i and j) cyanobacteria-like microfossils (She et al., in preparation). In Fig. 2e, a sinuous tubular filament extends outwards from the innermost part of the granule, cross-cutting boundary zones. In many cases, microfossils are closely associated with the intra-granular zoning (Fig. 2g, i and j). In Fig. 2g, the granule is dominated by a large population of more than 1000 coccoidal microfossils, each of which is about 8 μm in diameter (Fig. 2h and inset). Fig. 2i and j show a granule with a brownish core surrounded by filamentous microfossils. The core consists largely of coccoidal microfossils ~5 μm in diameter, most of which possess a submicron-sized black central "spot" (Fig. 2j, white arrows). In the filamentous film, tubular filaments 2–3 μm in diameter are mostly oriented tangentially to the surface of the core as shown by the observed transverse and longitudinal sections although some radially-oriented ones are also present (Fig. 2j, black arrows).

4.1.2. The cements

Two generations of cements are observed in the Doushantuo phosphorites. The first generation is micro-laminated isopachous or botryoidal apatite (IA) which rims granules composed of submicron-sized apatite (SA) (Fig. 2k and l). Rims of adjacent granules often have the same thickness and number of laminae. These microcrystalline cements show undulatory extinction and typically range in thickness from 15 μm to 40 μm. A second generation of cement consists of mosaic quartz which occupies interstitial spaces (Fig. 2k). In more diagenetically-altered samples, however, quartz cement grew into mm-sized crystals replacing isopachous apatite cement (Fig. 2m).

4.1.3. Other diagenetic minerals and textures

Four types of sulfidic fabrics occur in the Doushantuo phosphorites. The first type, associated with microfossils, consists of anhedral grains which have directly replaced both the envelopes and internal degraded structures of the organic remains (Fig. 2n). A second type occurs as rare discontinuous laminae of submicron-sized particles in the isopachous cement (Fig. 2o). The third type is present in interstitial spaces as euhedral to subhedral grains. They can occur as single crystals, clusters or chains, and can be locally quite abundant (Fig. 2p). In many samples, iron oxides or hydroxides are present. Some of these still preserve a core of sulfide, although all of them probably represent the later oxidative replacement of diagenetic sulfides. The last type of sulfide fabric includes ambient inclusion trails (Wacey et al., 2008) which show the migration of sulfide grains or their oxidized pseudomorphs (Fig. 2q–s). In Fig. 2q, longitudinal striations can be seen behind a euhedral pyrite grain which migrated from phosphatic matrix toward a granule. Fig. 2r and s show a ~350-μm long and ~20-μm wide trail terminating with a hexagonal hematite (limonite?) crystal of same diameter as the trail. The trail, itself, appears to consist of two segments whose overall path parallels the contour of the granule (Fig. 2r).

Carbonate minerals occur in the upper part of the phosphorite sequence where banded phosphorites are intercalated with carbonates. In Fig. 2m, carbonate minerals have partially replaced both quartz and apatite cements, in addition to phosphatic granules. In some cases, they have completely erased the primary mineralogy and textures. Clear euhedral to subhedral feldspars are also observed as clusters or single crystals within the granules (Fig. 2t). The feldspars are 10–50 μm in length and show first-order gray to white interference colors. They have the typical crystal habit of feldspars although no twining was observed.

Early diagenetic compaction appears to have changed the shape of the some granules. This can be seen in Fig. 2u, where a detrital quartz grain indents a phosphatic granule, which appears to have been incompletely lithified at the time.

4.2. Ultrastructures revealed by SEM

SEM studies of freshly broken surfaces of the granular phosphorites revealed distinct features of granules and cement (Fig. 3a–e). Granules themselves are composed primarily of randomly-oriented apatite nano-crystals with some rosette-like fabrics occurring locally. Most of the crystals are elongated prisms with widths of ~50 nm and lengths of 150–500 nm (Fig. 3b). Cements between the phosphate granules, however, are characterized by the radially-oriented, elongated prisms with widths ranging from 100 to 150 nm and lengths up to 1 μm (Fig. 3c). These are consistent with undulatory extinction observed under the optical microscope. Apatite crystals with similar textures also occur as botryoids on the surface of coated granules or in interstitial pores (Fig. 3d and e). They are occasionally observed in interstitial spaces but never in the interior of the granules. In the BSE image of one granule (Fig. 3f), micron-sized euhedral albite grains, embedded in apatite groundmass, are observed, consistent with microscopic observations. EDS analyses show that the bright phase in the cracks in Fig. 3d is barite (Fig. 3g), whereas the feldspars in the granule (Fig. 3f) are nearly pure albites without detectable calcium or potassium (Fig. 3h). Detection of carbon and fluorine in the apatite cement (Fig. 3i) indicate that carbonate fluorapatite, the dominant mineral of typical marine phosphorites, characterizes the mineralogy of the Doushantuo phosphate.

4.3. Raman microspectroscopic documentation of composition and textures

Raman microspectroscopic analyses revealed disseminated CM in both the phosphate groundmass and microfossil-like structures. The granules are largely composed of apatite although diffuse particulate CM is also present in most areas as indicated by hyperspectral images and D- and G- bands in the Raman spectra (Fig. 4 a, b and i). The CM-rich areas appear to correspond to the browner zones in the transmitted light image but a one to one comparison is not evident. Relatively well-preserved microfossils (Fig. 4c) often display carbonaceous vesicles with strong D-band and G-band intensities (Fig. 4d and i). Submicrometer-sized CM particles are ubiquitous throughout the apatite groundmass within the granules (Fig. 4b, d and f). In the isopachous cements that rim the granules, however, CM is almost undetectable (Fig. 4d and f).

Raman spectra of CM in the phosphorites are characterized by broad D-band (disordered CM) and G-band (graphitic CM) with similar intensities. D-bands are nearly symmetric and centered between 1340 and 1362 cm^{-1} (average 1350 cm^{-1}) with widths

abundant coccoidal microfossils, (h) enlarged view of the coccoidal microfossils in (g), (i) a concentrically-zoned elliptical granule displaying a yellowish core colonized by filaments, (j) enlarged view of the filamentous microfossils in (i) showing black particles inside coccoids (white arrows) and tangentially- and radially-oriented filaments (black arrows), (k) isopachous apatite cement (IA) rimming submicron-sized apatite granules (SA) and interstitial quartz cement (qtz), (l) fine laminae in IA, (m) granules (SA) cemented by mm-sized quartz cement (qtz) which, in turn, was replaced by sparry carbonate (carb), note the corrosion and replacement of SA by carbonate minerals (arrows), (n) pyritized coccoidal microfossils, inset showing enlarged view under transmitted light, (o) IA containing concentric opaque laminae (arrows), (p) interstitial pyrite cluster, (q)–(s) ambient inclusion trials (AITs): (q) An euhedral pyrite migrated into a granule, note the tailing; (r)–(s) an ambient inclusion trial in the margin of a granule, showing a "head" of hematite (limonite?) followed by a curved trail with a visible length of ~350 μm, (t) a cluster of feldspars in the core of an asymmetrically-zoned granule and (u) a granule indented by a detrital quartz (arrow). (For interpretation of reference to color in this figure legend, the reader is referred to the web version of this article.)

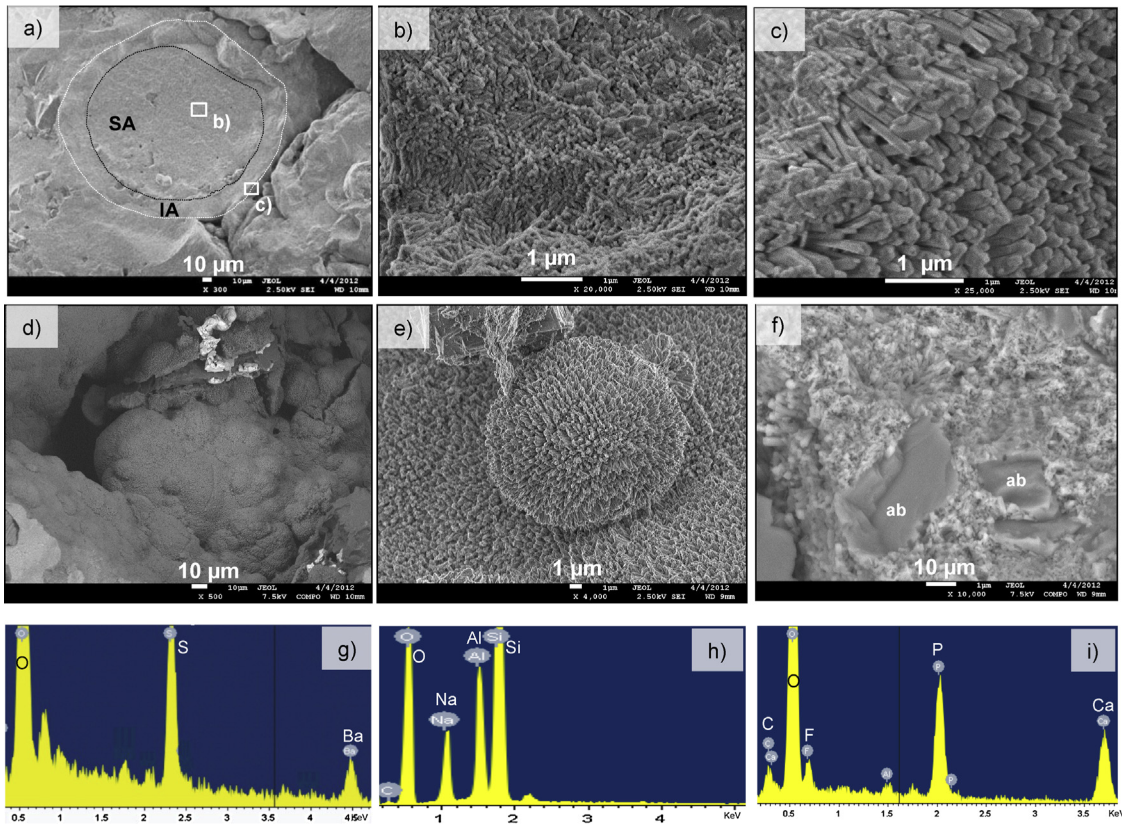

Fig. 3. Secondary electron images (SEI) (a)–(e), backscattered electron image (BSE) (f), and EDS spectra (g)–(i): (a) Phosphatic granule (SA) with a isopachous apatite rim (IA), squares show the locations of magnified views in (b) and (c), (b) randomly oriented submicron-sized apatite crystals (SA), (c) prismatic apatite crystals (IA) oriented perpendicularly to the surface of granule, (d) apatite botryoids grown on pore surface, (e) magnified view of a phosphatic botryoid, (f) euhedral albites embedded in apatite groundmass. EDS spectra: (g) the bright phase (barite) in (d); (h) feldspar in (f); and (i) botryoidal apatite cement in (d).

(FWHM, full width at half maximum) ranging from 77 cm^{-1} to 135 cm^{-1} (Table 1). For most analyses, D-bands are noisy and sometimes multifurcate into a few unidentified peaks, whereas G-bands are generally asymmetric and inclined to the low-frequency side (Fig. 4i). The centers of the G-bands vary between 1588 cm^{-1} and 1622 cm^{-1}, with an average at 1605 cm^{-1}. The band widths (FWHMs) are 45 to 89 cm^{-1}, smaller than those of the D-bands.

For the apatite groundmass within the granules, Raman spectra are characterized by a sharp apatite peak at ~965 cm^{-1} and ubiquitously associated D-bands and G-bands of finely disseminated CM with relatively low intensities (Fig. 4i), consistent with the Raman hyperspectral images (Fig. 4b, d, f and h). These, together with the brownish color of the granules observed under polarized transmitted light, confirmed the ubiquitous presence of finely disseminated CM within all phosphate granules.

In some cases, submicron-sized pyrite grains form discontinuous opaque laminae within the granule cements (Fig. 4e and f). Replacement of microfossils by pyrite is common and can be observed in Fig. 4g and h. The presence of pyrite associated with the septate filament is demonstrated by Raman peaks at ~345 cm^{-1} and ~380 cm^{-1} (Fig. 4i).

The degree of graphitic order is indicated by Raman spectral parameters which record peak metamorphic conditions and remain unaffected by retrogression; the temperature of CM has been calibrated against metamorphic mineral assemblages in metasediments (Beyssac et al., 2002; Lahfid et al., 2010). Using the Lahfid equations derived for low-grade metasediments, we calculated the peak metamorphic temperatures of the CM in the Doushantuo samples. Temperatures calculated by both equations agree well for the same analysis, but shows large variations for different analyses and define a broad range between 217 °C and 360 °C. These are slightly higher than the estimation of a maximum burial depth of 4 km (Bristow et al., 2009; Jiang et al., 2006) for the whole Doushantuo Fm which is generally considered as unmetamorphosed but roughly constrains the upper limit of thermal evolution of the formation.

4.4. Occurrence and associations of CM and apatite within microfossils documented by FIB-TEM studies

A FIB foil (TP0901S_09) extracted *in situ* from a colony of coccoidal microfossils (Fig. 5a) in thin section was studied using TEM and EDS to reveal the processes of mineralization and preservation of microfossils. The FIB foil is 10 μm × 10 μm in dimension (Fig. 5b) and locally electron-transparent (Fig. 5c). Imaging of the foil revealed a complex internal ultrastructure of the microfossils (Fig. 5d, e and f) now composed of apatite and CM (Fig. 5g). Electron-dense apatite nano-crystals occur in two types. In the first type, elongated acicular apatite crystals about 70–90 nm wide are radially aligned and form densely-packed clusters that are ~1.5 μm apart (Fig. 5d and f). Comparisons of optical microscopic and Raman hyperspectral images suggest that they are probably filling the internal spaces of dehydrated cells. The second type of apatite, with variable sizes from ~500 nm to ~100 nm, tends to occur as individual crystals in electron-lucent groundmass (Fig. 5d). Most of the type 2 crystals are located in between the vesicles of the coccoids and have hexagonal shape (basal section) that indicate a different crystallographic orientation, compared to the type 1 apatite (Fig. 5d and f). The electron-lucent areas between apatite crystal clusters, however, exhibit somewhat amorphous, globular ultrastructure (Fig. 5e). The globules (vesicles) range in diameter from 20 to 80 nm and are enclosed by electron-dense envelopes

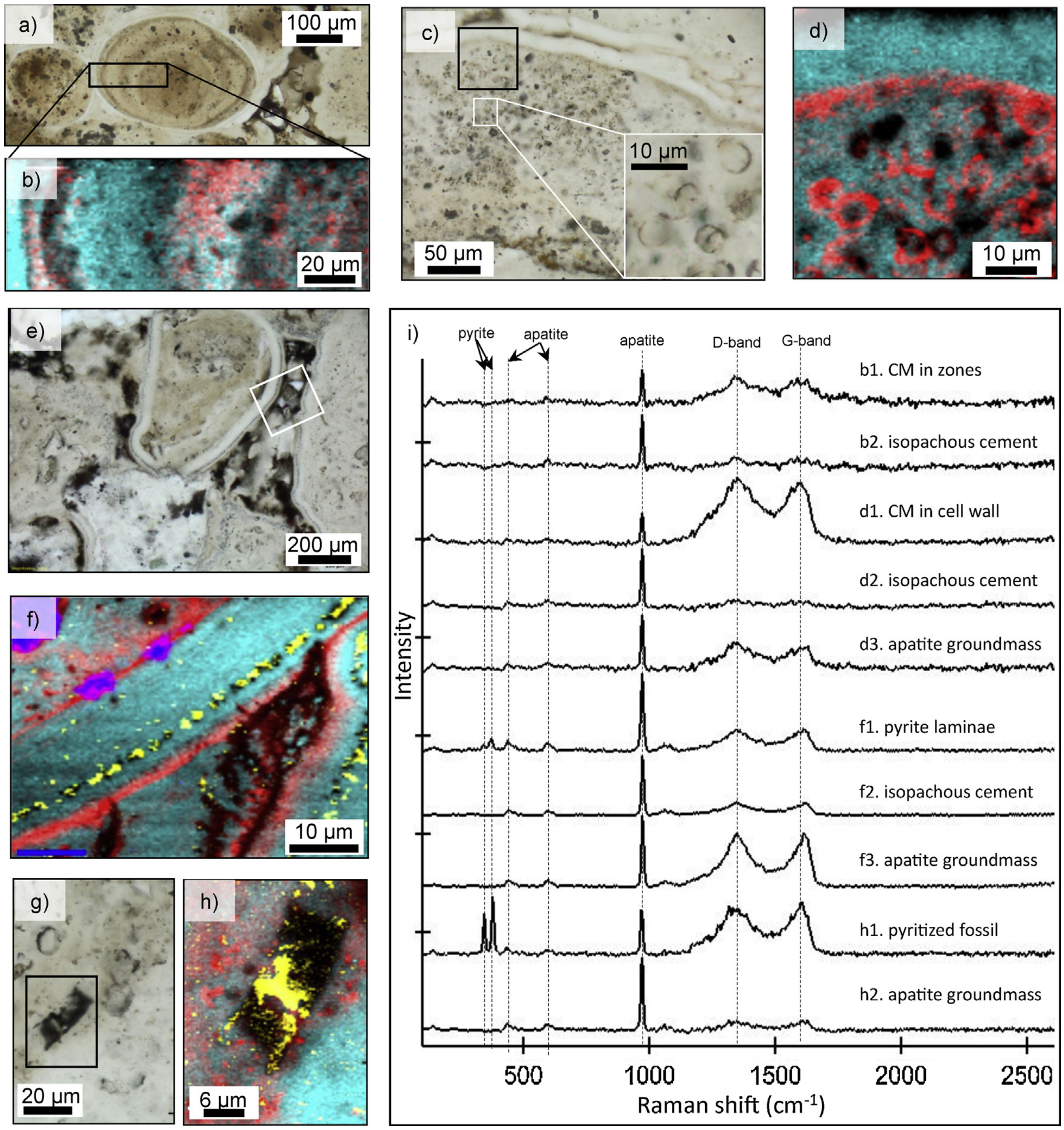

Fig. 4. Representative Raman images and average spectra: (a), (c), (e) and (g) transmitted light images of targets for Raman imaging, (b), (d), (f) and (h) Raman hyperspectral images of apatite (turquoise), CM (red), quartz (blue), pyrite (yellow) and poor Raman signal (black) for the marked areas in (a), (c), (e) and (g), respectively and (i) average Raman spectra of CM, apatite and pyrite of various occurrences.

about 3 nm thick. EDS analyses document that they are composed of carbon (Fig. 5g), which corresponds to the CM shown in Raman images (Fig. 5a). This globular ultrastructure appears similar to that reported by Bernard et al. (2007), as characterizing the outer wall of fossil lycophytes megaspores, and probably represents degraded original cell walls in this case.

4.5. Elemental composition and distribution in microfabricated microfossils

NanoSIMS chemical imaging was conducted on two FIB foils, TP0901S_09 and TP0901S_12b, as well as on the thin section from which the FIB foils were extracted. TP0901S_12b was extracted within a granule containing abundant filamentous microfossils (Fig. 6a). The dark filaments visible on the secondary electron image represent segments of the microfossils. Compositional maps show a generally uniform presence of ^{16}O, ^{31}P and ^{32}S throughout the FIB foil, although the slightly beveled geometry of the foil yields a secondary ion gradient across the images (Fig. 6a and b). Notably, at the upper center of the foil (Fig. 6a), a small zone containing both ^{12}C and ^{14}N is observed, which is consistent with the presence of kerogenous material associated with the filamentous microfossils that are clearly visible on the secondary electron image. Moreover, two small hotspots are present on the ^{32}S map at the same area. The ^{12}C^{1}H map, compared with the ^{16}O and ^{31}P maps, also showed the presence of trace amount of carbon closely intermixed with phosphatic groundmass (carbonate fluorapatite).

The FIB foil TP0901S_09 was rethinned after TEM analysis as it was only locally electron-transparent (Fig. 5c) and this caused partial damage of the foil (Fig. 6b). NanoSIMS elemental maps (Fig. 6b) show the ubiquitous presence of ^{16}O and ^{31}P, as expected for apatite, but also of ^{32}S, which suggests the presence of phosphate-associated sulfate. Although the cause of unusually high ion yields for ^{12}C^{-}, ^{12}C^{1}H^{-} and ^{12}C^{14}N^{-} is uncertain, the parallel variations of C and CN are evident. Moreover, there appears to be a one-to-one correspondence of carbon and nitrogen with

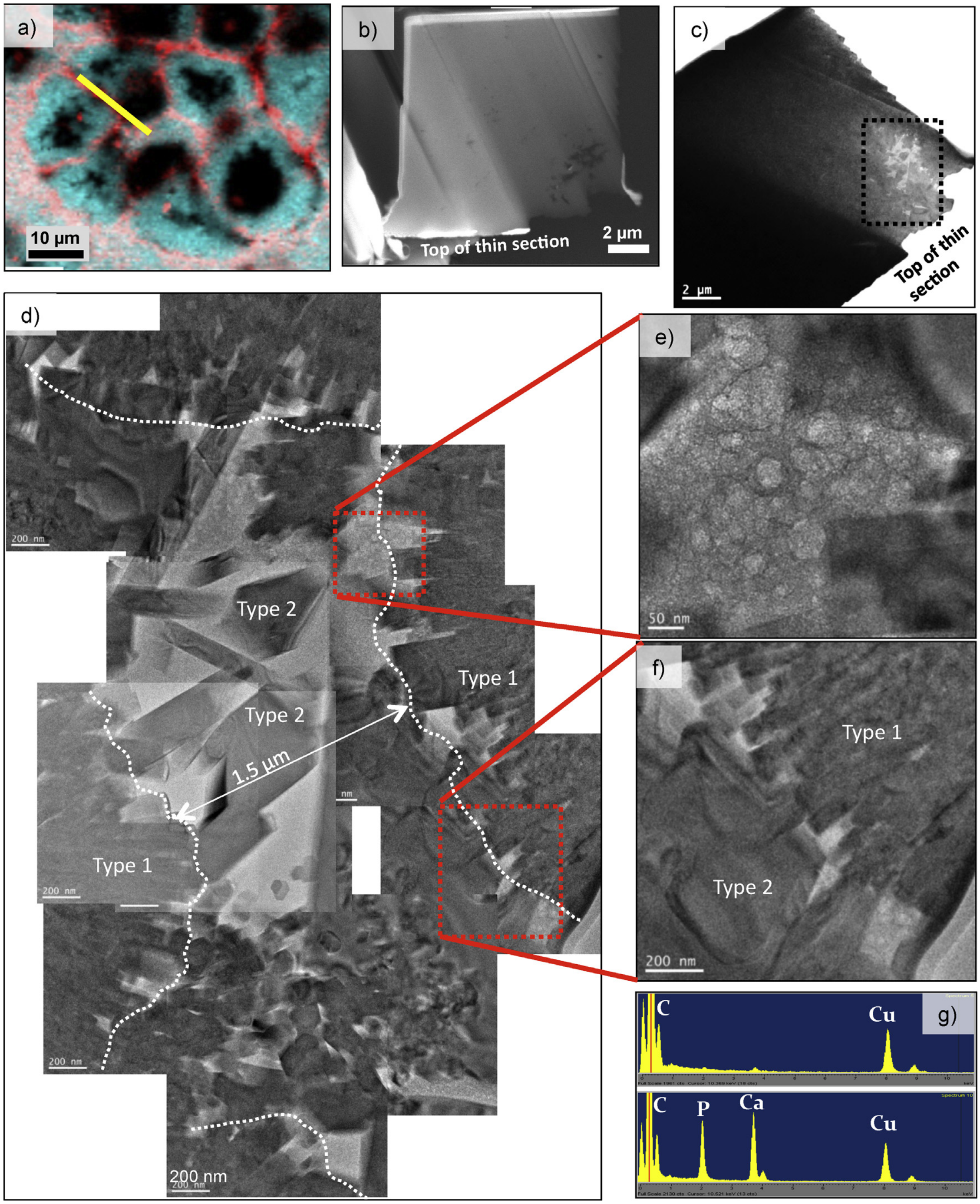

Fig. 5. TEM images and EDS spectra of a FIB foil (TP0901S_09) extracted from thin section TP0901S: (a) Raman hyperspectral image of a colony of coccoidal microfossils (color codes same as Fig. 4), the yellow line shows the target for focused ion beam (FIB) milling. (b) FIB foil TP0901S_09 (SEI), (c) transmitted electron microscopic (TEM) image of the foil, dashed square shows the location of (d), (d) mosaic of TEM images showing electron-dense apatite crystals and electron-lucent areas, (e) electron-lucent area consisting of carbonaceous globules, (f) Radially-oriented acicular apatite nanocrystals (type 1) and basal section of a larger apatite crystal (type 2) and (g) EDS spectra of carbonaceous nanoglobule (upper) and apatite crystal (lower). (For interpretation of reference to color in this figure legend, the reader is referred to the web version of this article.)

the cellular structure shown in the secondary electron image (the lower corner). The localized linear charged zones on the ^{12}C and ^{12}C^{1}H chemical images are likely due to geometric artifacts from the micro-fabrication.

Elemental maps of a spheroidal microfossil (Fig. 6c) in thin section TP0901S revealed the presence of remnant organic matter associated with cell structure. On the ^{12}C and ^{12}C^{1}H maps, discontinuous clots are observed, roughly corresponding to the CM-rich areas on the transmitted light image (darker) and the reflected light image (brighter). The cell structure is best observed in the ^{12}C^{14}N map, which reveals a low intensity, thin organic-rich zone corresponding to the cell boundary. The correlation between the elemental maps and the transmitted and reflected light images rules out significant surface contamination. The heterogeneous distribution of ^{16}O reflects the topography of the sample surface. ^{31}P appears to be inversely correlated with carbon (and associated H and N), which is consistent with the wane and wax relationship between organic matter and phosphate groundmass. The

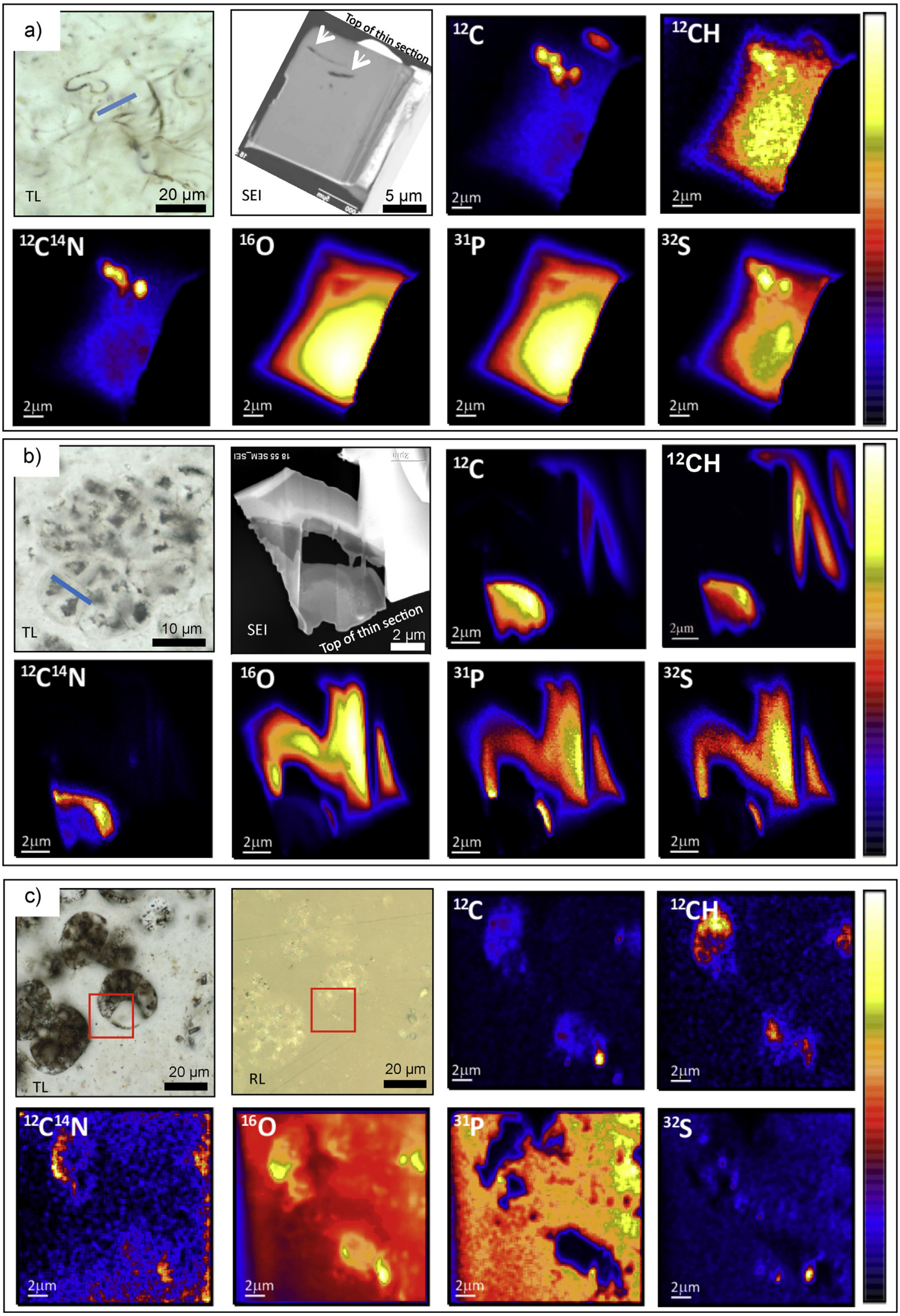

Fig. 6. NanoSIMS elemental maps (of ^{12}C, $^{12}C^{1}H$, ^{16}O, $^{12}C^{14}N$, ^{31}P and ^{32}S) for FIB foils TP0901S_12b (a) and TP0901S_09 (b) and thin section TP0901S (c). Photomicrographs (TL: transmitted light, RL: reflected light) and secondary electron images (SEI) show the context of the targets. For (a) and (b), the lines on the TL images indicate the location where the FIB foils were extracted. Note the filaments (white arrows) on the secondary electron image of (a). Color bars on the maps indicate relative intensity of NanoSIMS response.

Table 1
selected Raman spectral data of CM of various occurrences in four thin sections of the Doushantuo phosphorites.

Sample	Description of target	Depth of scan (μm)	G-band position	G-band FWHM	D-band position	D-band FWHM	D-band area	G + D2 band area	D intensity	G intensity	D/G (intensity)	T 1[a]	T2[a]
TP0901S	Cell wall of coccoids	0.8	1592.1	81.8	1342.5	106.5	4236	2945	129	121	1.07	268	260
	Cell wall of coccoids	3	1598.3	81.1	1353.4	135.4	3639	2105	166	162	1.03	322	324
	Cell wall of coccoids	5	1613.1	75.1	1352.7	116.6	1932	1205	83	87	0.96	300	296
	CM in apatite groundmass	4	1615.6	45.2	1357.1	88.9	672	407	27	28	0.97	309	307
	Sheath of a filament	6	1609.2	80.1	1356.8	114.5	2381	1493	104	99	1.05	299	294
	Sheath of a filament	1.5	1589.6	89.0	1360.3	120.8	3870	2407	183	182	1.00	301	297
	Cell wall of coccoids	3	1592.7	78.0	1351.2	132.8	1018	539	624	630	0.99	348	360
TP0901	Colonial coccoids	1	1605.4	77.3	1361.2	95.9	3388	2717	488	518	0.94	224	217
	CM in apatite groundmass	3	1589.1	79.4	1348.5	111.0	5176	2933	229	224	1.03	328	332
	CM in feldspar	3	1607.2	76.8	1346.7	102.3	5185	3625	462	460	1.00	266	258
TP0902	Cell wall of coccoids	1	1609.4	75.1	1342.4	90.1	2000	1448	349	352	0.99	255	247
	CM in apatite groundmass	1	1609.9	73.7	1340.3	89.6	1588	1220	130	136	0.95	237	229
	CM coating on cement	1.5	1612.6	55.6	1344.9	91.9	723	450	317	315	1.01	301	297
	Sheath of a filament	10	1605.4	72.6	1346.7	108.3	2797	1799	327	340	0.96	291	286
	Cell wall of globular microfossils	1.5	1594.5	71.9	1341.3	110.6	11,862	8013	906	952	0.95	276	269
TP0906	CM in microfossil	0.5	1620.8	45.2	1352.5	85.4	1624	916	77	69	1.12	329	334
	CM layer in cement	1.5	1621.7	44.6	1355.7	77.4	1595	922	71	68	1.05	322	324

[a] T1 and T2 are temperatures calculated using the equations proposed for low-grade metasediments by Lahfid et al. (2010).

apparent correlation of ^{32}S and ^{12}C hot spots, however, suggests the sulfur detected here is associated directly with the CM, consistent with the commonly observed pyritization of microfossils. The dispersed ^{32}S in the apatite groundmass, however, might represent phosphate-associated sulfate that is in trace amount but ubiquitous. The heterogeneous distribution of ^{16}O and overall low intensity of ^{32}S are likely due to sample surface topography. This, compared with Figs. 6a and b, demonstrate the power of FIB-based micro-fabrication to achieve smooth sample surface.

Overall, the close correspondence of C and N distributions within the carbonaceous structures imaged by optical microscopy, Raman spectroscopy, and SEM lend strong support to the biological origin of these structures.

5. Discussion

5.1. Formation of the granules by accretionary growth

At the present time, there is no consensus on the origin of granular phosphorite, although several models have been proposed: (1) reworking of previous phosphate deposits (*e.g.*, Föllmi, 1996); (2) *in situ* formation within microbial mats (Dahanayake and Krumbein, 1986); (3) vadose transformation of microbially constructed mudstone phosphorite (*e.g.*, Soudry and Southgate, 1989); (4) *in situ* diagenetic mineralization driven by changes in pore-water redox potential (*e.g.*, Pufahl and Grimm, 2003); (5) replacement of biogenic grains (*e.g.*, Birch, 1980; Manheim et al., 1980); and (6) abiogenic accretionary (*i.e.*, oöid-forming) processes whereby apatite is precipitated onto the surface of a nucleus in water saturated or supersaturated with respect to calcium phosphate (Swett and Crowder, 1982; Zhao, 1989). None of these previous models provides a satisfactory explanation of the characteristics of the Doushantuo phosphorites studied here.

The primary sedimentary nature of the Doushantuo granules is clearly reflected in their concentrically zoned fabric. Such zonation is inconsistent with simple disruption, reworking and transport of partially lithified muds. The small crystal size of apatite in individual granules combined with the absence of relict carbonate mineral grains argue against formation by replacement of carbonate precursors. Sedimentological evidence for high energy environments (such as ripple marks, cross-beds, and other detrital fabrics) is generally lacking in these deposits. Some reworking of some of the granules is apparent, however, indicating a hydrologic regime that was capable of moving these grains within the sediment. The granules are cemented by isopachous apatite and interstitial quartz, neither of which exhibits fabrics indicative of the former presence of microbial mats. Absence of a single exotic nucleus in most granules and the generally small but variable grain sizes argue against an oöid-like origin. Similarly, the Doushantuo granules cannot be explained by vadose transformation either because of the distinct textures and the fact that no convincing evidence of subaerial exposure for all the granular phosphorites is observed. Pufahl and Grimm (2003) ascribed all Phanerozoic coated phosphate grains to either unconformity-bounded (UB) or redox-aggraded (RA) grains based on a study of granular phosphorites from differing ages and locations. The Doushantuo granules, however, do not fit in either of these categories because they have oncoid-like microstructures and show no evidence of graded redox shifts in their internal mineralogy.

We thus interpret the Doushantuo granular phosphorites were formed by microbially-mediated accretionary growth. Populations of different coccoids and filaments, of undisputed biological origin as documented by optical microscopy, Raman microspectroscopy, SEM, TEM and NanoSIMS, are abundant and distributed throughout many of the granules. Some granules show colonization of filaments around a core of degraded coccoids (Fig. 2i and j), whereas others consist of large populations of coccoids that constitute the majority of granules (Fig. 2g and h); both of which suggest a genetic link between the microfossils and the granules. The characteristic zonation reflects compositional variations, such as contents of CM (Fig. 4b), and represents primary growth laminae. Some asymmetrically-zoned granules contain abundant oriented filaments, which points to *in situ* benthic growth on the seafloor from a microbial phosphatic ooze.

Overall, these observations are consistent with the idea that granule growth was a primary environmental or very early diagenetic feature associated with microbial growth and production of excess extracellular polymeric substances (EPS). We propose a new model in which EPS served as a primary substrate that defined the laminated character of the zoned granules. These laminae, or zones, were in some cases re-colonized, leading to differences seen in their biological composition. In studies of wastewater treatment, the formation and stabilization of biogranules by microorganisms and associated EPS has been widely documented (Liu et al., 2004; Sheng et al., 2006). The internal structures of the Doushantuo granules and their close association with microfossils are similar to the zoned accretionary structures documented in extant microbial sludge flocs (Sheng et al., 2006), which supports our bio-accretionary model. Subsequent mineralization during early diagenesis in such phosphate-rich benthic settings allowed for the formation of cryptocrystalline apatite within granules and the subsequent rim growth and cementation to form fully lithified phosphorites.

5.2. Role of microorganisms and EPS in the precipitation of calcium phosphate

Biological involvement in phosphogenesis has previously been thought of as an intermediate process that transported phosphorus from the photic zone to the seafloor or released phosphorus from organic matter to ambient water (*e.g.*, Papineau, 2010). Southgate (1986) noted that filamentous microorganisms promoted the precipitation of phosphate by providing both a source of phosphate to the pore water and a substrate on which phosphate preferentially nucleates. Cyanobacteria and associated EPS, in particular, are able to promote precipitation of carbonate minerals through the bacterially-influenced precipitation of $CaCO_3$ within Cyanobacterial EPS (Obst et al., 2009). Riding (2006) showed that photoautotrophs may cause a localized increase of pH, which in turn can trigger precipitation of carbonate. Adsorptive properties of EPS have been well documented, especially in terms of biosorption of pollutants and toxic ions (Beech and Cheung, 1995; Loaëc et al., 1997). EPS which possesses abundant anionic carboxyl and hydroxyl groups can provide binding sites for metals and can chelate seed particles that act as nuclei for carbonate precipitation (Jimenez-Lopez et al., 2011; Knorre and Krumbein, 2000). The fibrous nature of EPS has been observed to form reticulate patterns that match the lattice geometry of hexagonal to trigonal crystallographic systems (Sanz-Montero et al., 2008). Consequently, EPS is expected to have the potential to actively control the precipitation of apatite. In fact, biological removal of phosphorus has been widely used in wastewater treatment. Previous workers have attributed the removal of phosphorus to the actions of polyphosphate-accumulating organisms (PAOS), which can uptake phosphorus from activated sludge much more efficiently than their metabolic demand (Mino et al., 1998). The role of EPS in phosphorus removal may account for half of all phosphorus removed from activated sludge (Cloete and Oosthuizen, 2001; Liu et al., 2006). We propose that similar processes were responsible for the phosphatization of the Doushantuo granules.

Textures and ultrastructures of the phosphatic granules are consistent with biologically-mediated precipitation of calcium phosphate. Random orientation and small sizes of the apatite crystals in the granules are consistent with the rapid precipitation within zones of EPS, providing numerous nucleation sites, but simultaneously, limiting the space available for the growth of larger apatite crystals. In contrast, cements nucleated outside the EPS-rich granules formed larger isopachous and botryoidal textures growing into EPS-free space. Finely disseminated CM, which is ubiquitous throughout the granules as documented by Raman microspectroscopy, likely represents remains of the degraded EPS. This CM is generally absent in cements, which is consistent with our EPS model because cement is precipitated during later diagenesis from pore water solutions. Microorganisms, in addition to the EPS, also effectively controlled precipitation of phosphate within their cells. This is suggested by the TEM ultrastructures of different types of apatite nano-crystals that are closely associated with cellular morphology, consistent with the observation of calcium phosphate precipitated by cultivated bacteria (Benzerara et al., 2004).

Our model (Fig. 7) emphasizes the role of cyanobacteria EPS in the formation of phosphorite because cyanobacteria dominate the Doushantuo assemblage (She et al., in preparation). In the shallow-marine photic zone with high nutrient availability, actively dividing cyanobacterial cells produce copious amounts of EPS. This leads to the agglomeration of cells and detrital particles during granule formation. At the water-sediment interface where phosphorus availability is high, rapid precipitation of calcium phosphate within the granules is promoted by chemical gradients created by the microbes and abundant nucleation sites provided by EPS in the collective microbial glycocalyx. During intermittent nutrient-limited periods, microbial activity is much lower and finely-laminated phosphorites are formed by slow deposition and subsequent phosphatization of tiny released polymeric substances (RPS) (Fig. 7).

5.3. Microbial sulfate reduction

Sulfur-bearing phases are common in phosphorites and associated rocks (Arning et al., 2009; Benmore et al., 1983). In this regard, the activity of sulfur-metabolizing microorganisms has been invoked as the major cause of the release of phosphorus and subsequent formation of phosphorites (Bailey et al., 2007; *e.g.*, Schulz and Schulz, 2005). Benmore et al. (Benmore et al., 1983) reported sulfur isotopes of structurally-bound sulfate in phosphorite, which suggested phosphorite formation both within the sulfate-reducing zone and between the sulfate-reducing and overlying oxic conditions. Based on S isotopic systematics of sulfides and biomarkers, Arning et al. (2009) proposed that combined activities of sulfate-reducing bacteria and sulfide-oxidizing bacteria played important roles in the formation of phosphatic laminites.

In the Doushantuo samples, numerous occurrences of sulfides were observed, including pyrite associated with microfossils, microcrystalline pyrite laminae in isopachous cement, largely oxidized euhedral pyrite clusters filling interstitial spaces, and AIT-forming pyrites. The presence of pyritized microfossils suggests that the first generation of microbial sulfate reduction (MSR) might have occurred before obturation of the post-mortem microorganisms by complete phosphatization. This is consistent with the observation that many microfossils are more or less degraded even though they are embedded in the phosphatic groundmass that were barely affected by recrystallization. The ubiquitous presence of sulfur in the phosphorite granules and its close correspondence to phosphate, as documented by the NanoSIMS elemental mapping, suggest that the sulfur is present as structurally-bound sulfate that is derived from seawater (Nathan and Nielsen, 1980; Shen et al., 1998; Shields et al., 1999). This sulfate, along with the microorganisms and EPS, likely provided reactant for the early sulfate reduction

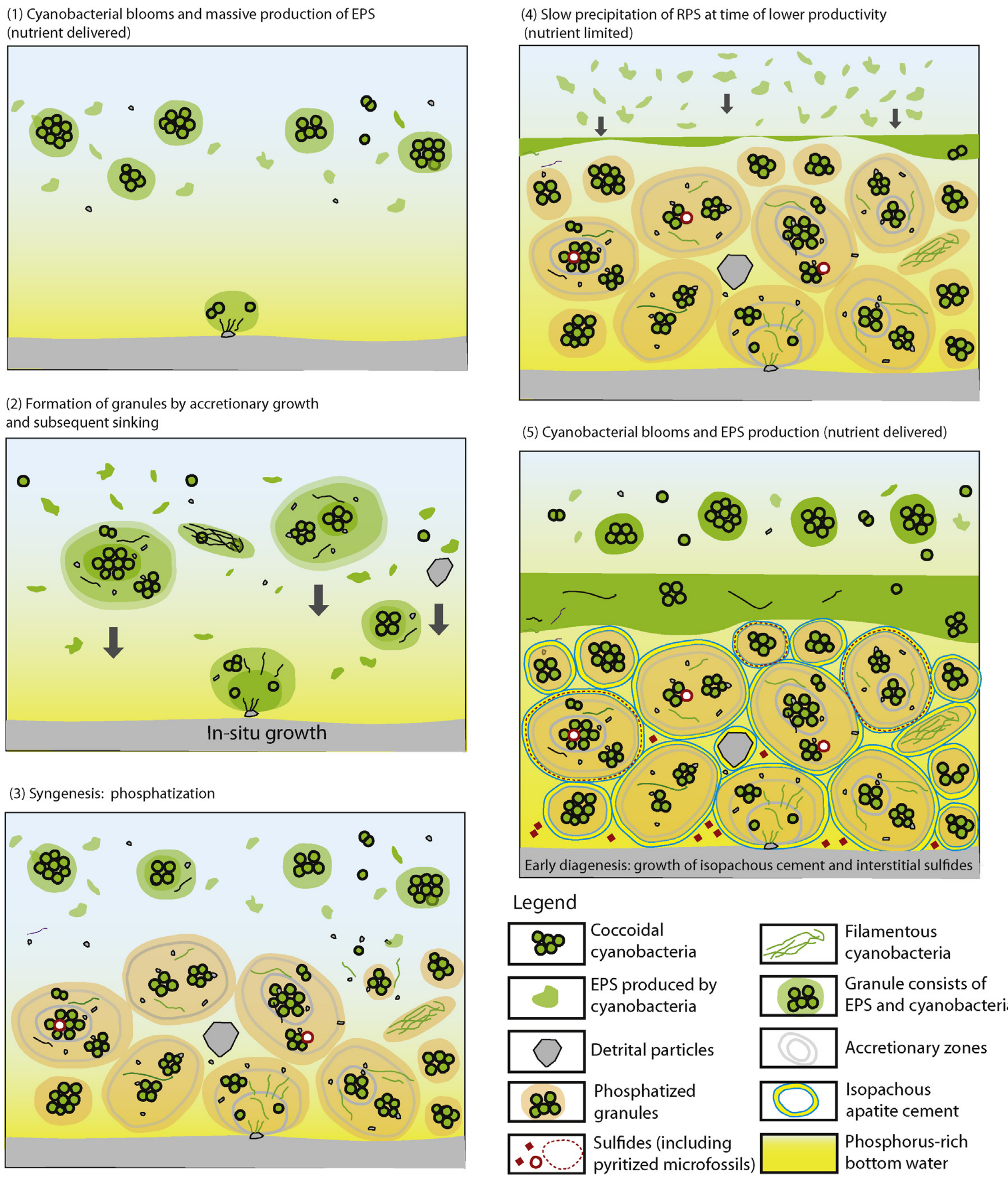

Fig. 7. A model envisaging the formation of the Doushantuo granular phosphorites.

within the granules probably during syngenesis while phosphatization was still in progress.

Occurrence of fine pyrite laminae in the isopachous cement around the granules points to a second generation of MSR, which is followed by the latest generation of MSR that produced the interstitial and AIT-forming sulfides. Although various hypotheses have been proposed to explain the formation of AITs (Knoll and Barghoorn, 1974; Lepot et al., 2009, 2011; McLoughlin et al., 2010; Tyler and Barghoorn, 1963; Wacey et al., 2008), all these models require a low permeability to allow pressure to build up locally or concentrate organic acids formed by decomposition at the tip of a growing micropit. This seems unlikely for a granular rock because it often contains many interstitial pores. However, with the presence of intercalated massive or finely-laminated sub-micron sized phosphatic layers presumably formed by released polymeric substances (RPS) during intermittent periods of cyanobacterial blooms (Fig. 7), it is possible to locally achieve the low permeability required for AIT formation.

It should be noted, however, that a major role of MSR in the phosphatization of the granules is not favored for the Doushantuo samples as most sulfides clearly postdate the formation of the phosphatic granules. Moreover, most of the observed microfossils share many features with cyanobacteria rather than S-metabolizing species (She et al., in preparation), consistent with a dominant role of cyanobacteria and their EPS in phosphate mineralization. Formation of sulfides has mainly taken place in anoxic pore waters during burial diagenesis, which generated clusters of euhedral sulfides in interstitial space.

5.4. Other diagenetic processes

Other diagenetic processes include compaction, pressure dissolution, quartz cementation and albitization. Textures indicative of compaction and pressure solution of the granules are frequently observed. Dissolution of the granules might have delivered phosphate, sulfate and organic matter into pore water solutions, which likely assisted subsequent formation of the isopachous cement and the continuation of microbial sulfate reduction. This might also have facilitated the formation of AITs by decreasing the permeability of the granular rock. As the latest generation of cement, interstitial quartz attests to significant changes in later pore water chemistry as supersaturation of silica is most easily reached under acidic conditions rather than nearly neutral or slightly alkaline conditions required for apatite and carbonate precipitation. Silica precipitation probably occurred at depth following later burial diagenesis. Replacement of quartz and apatite cement by carbonate minerals, which is observed in many samples, is probably related to later influx of carbonate-rich fluids. This is consistent with the macroscopic change seen in field outcrops of the Doushantuo sedimentary sequence from interbedded phosphorites and black shales to the carbonate-phosphorite assemblage along with the subsequent demise of phosphorite deposition. During late diagenesis or modern exposure, oxidation of the rock led to partial or complete conversion of sulfides into iron oxides and sulfates that likely escaped in solution.

As a minor mineral phase, euhedral albite occasionally occurs as either cluster or individual crystals in the phosphatic granules. Their euhedral shape and chemical purity (high Ab component) point to an authigenic origin (Kastner and Siever, 1979). Authigenic albite has been reported from carbonate rocks (Kastner and Siever, 1979; Rais et al., 2008; Spötl et al., 1999) and interpreted to be formed by paleobrine-carbonate reactions in deep-burial and incipient metamorphic settings (Spötl et al., 1999). Albitization of the Doushantuo phosphorites probably happened under similar conditions, but their close association with the phosphatic granules suggest that diagenetic changes of the phosphate and entrained mineral particles might have provided the required sodium, silica and aluminum.

6. Summary and implications

The Doushantuo phosphorites in Yichang are dominated by granular phosphorite. The granules are composed of submicron-sized apatite and generally display concentric to asymmetric zoning, defined, in part, by the presence of microfossils. Sulfides can be associated with microfossils, and they are also present in isopachous cement and can fill interstitial spaces. The granules are coated by isopachous apatite, which represents the first generation of early diagenetic cement. SEM observations showed that the granules are largely composed of randomly-oriented apatite nano-crystals, whereas the cement is characterized by radially orientated prismatic apatite. Backscattered electron images revealed the presence of numerous nanometer-sized carbonaceous particles, which are closely associated with the apatite nano-crystals. Raman microspectroscopic studies confirmed the preservation of highly disordered organic matter in microfossils and the systematic presence of disseminated CM in granules. Estimated metamorphic temperatures are consistent with those of lower greenschist facies metamorphism. TEM observations of a FIB foil documented two types of electron-dense apatite nano-crystals with one filling the internal space of cells and the other occurring as individual crystals in electron-lucent carbonaceous nano-globules interpreted to be the degraded remains of original cell walls. NanoSIMS elemental mapping of selected targets in FIB foils and thin sections revealed the presence of ^{12}C- and ^{14}N- bearing kerogenous material associated with the microfossils and trace amounts of carbon throughout the phosphatic granules. Sulfur is also observed as closely associated with phosphorus and oxygen and is interpreted as phosphate-associated sulfate in the phosphatic granules.

We propose a new model of a microbially-mediated nucleation and precipitation to explain the formation of the Doushantuo granular phosphorites. The abundance of microfossils and their close association with phosphatic granules document the importance of microbial activity granule formation. Extracellular polymeric substances (EPS), in particular, are crucial both for granule formation and early onset of phosphatization. The concentric and asymmetric zonings of granules are interpreted to have formed by accretionary growth, which occurred as microorganisms and other particles were aggregated by EPS. This happened both in the water column and on the sea floor. Rapid precipitation of calcium phosphate within granules is demonstrated by the random orientation and small size of the apatite crystals in the granules. Biogenic mucopolysaccharides might thus have provided both nucleation sites and constrained space for apatite crystallization. The presence of ubiquitous CM disseminated throughout the phosphatic granules is interpreted to represent the remains of the degraded polymeric substances, a feature that is missing from the surrounding cement.

The role of microorganisms in the precipitation of the Doushantuo phosphates is also suggested by TEM observation of the close association of different types of apatite nano-crystals with preserved cellular structure. This implies that initiation of phosphate crystallization was primary in the sense that it began prior to the complete decay and degradation of these microbes. This is in contrast to previously suggested links between microbial sulfate reduction/sulfide oxidation and the precipitation of phosphate, as most sulfide minerals postdate the bulk of phosphatization.

The combined use of multiple micro-analytical techniques for the petrographic characterization of texture, fabric and compositions of these rocks helps to both constrain and characterize the biological and geochemical processes involved in the origin and early diagenesis of granular phosphorite. In particular, correlated micro-analysis of phosphatic granules and microfossils using Raman microspectroscopy, SEM, FIB-TEM and NanoSIMS presents a powerful approach that can be used in future studies of various biomineralization processes and nanobiogeochemistry.

Acknowledgements

This work was supported by National Natural Science Foundation of China (grants 41272038 and 40802018), China Scholarship Council (grant 2010842016), Fundamental Research Funds for National Universities, China University of Geosciences (Wuhan), and the 111 Program for the Ministry of Education of China and the State Administration of Foreign Expert Affairs of China (grant B07039). DP acknowledges support from Boston College, the Carnegie Institution of Washington, NASA (the Astrobiology Institute and the Exobiology and Evolutionary Biology Program, grant numbers NNA04CC09A, NNX08AO16G, NNA09DA81A, and NNX12AG14G), and the Fond Québécois pour la Recherche sur la Nature et les Technologies. ZS and DP thank Xia Wen and Roger Mason for assistance in field trip, Shuhai Xiao and Shanrong Zhao for helpful discussion, Paul Boni for his mastery of thin section fabrication, and Dezhi Wang for help with TEM analyses.

References

Anbar, A.D., Knoll, A.H., 2002. Proterozoic ocean chemistry and evolution: a bioinorganic bridge? Science 297, 1137–1142.

Arning, E.T., Birgel, D., Brunner, B., Peckmann, J., 2009. Bacterial formation of phosphatic laminites off Peru. Geobiology 7, 295–307.

Bailey, J.V., Joye, S.B., Kalanetra, K.M., Flood, B.E., Corsetti, F.A., 2007. Evidence of giant sulphur bacteria in Neoproterozoic phosphorites. Nature 445, 198–201.
Beech, I.B., Cheung, C.W.S., 1995. Interactions of exopolymers produced by sulphate-reducing bacteria with metal ions. International Biodeterioration & Biodegradation 35, 59–72.
Benmore, R.A., Coleman, M.L., McArthur, J.M., 1983. Origin of sedimentary francolite from its sulphur and carbon isotope composition. Nature 302, 516–518.
Benzerara, K., Menguy, N., Guyot, F., Skouri, F., de Luca, G., Barakat, M., Heulin, T., 2004. Biologically controlled precipitation of calcium phosphate by *Ramlibacter tataouinensis*. Earth and Planetary Science Letters 228, 439–449.
Bernard, S., Benzerara, K., Beyssac, O., Menguy, N., Guyot, F., Brown Jr., G.E., Goffé, B., 2007. Exceptional preservation of fossil plant spores in high-pressure metamorphic rocks. Earth and Planetary Science Letters 262, 257–272.
Bernard, S., Beyssac, O., Benzerara, K., 2008. Raman mapping using advanced line-scanning systems: geological applications. Applied Spectroscopy 62, 1180–1188.
Beyssac, O., Goffé, B., Chopin, C., Rouzaud, J.N., 2002. Raman spectra of carbonaceous material in metasediments: a new geothermometer. Journal of Metamorphic Geology 20, 859–871.
Birch, G.F., 1980. A model of penecontemporaneous phosphatization by diagenetic and authigenic mechanisms from the western margin of southern Africa. In: Bentor, Y.K. (Ed.), Marine Phosphorites—Geochemistry, Occurrence, Genesis. Society of Economic Paleontologists and Mineralogists Special publication, Tulsa, pp. 79–100.
Bremner, J.M., 1980. Concretionary phosphorite from SW Africa. Journal of the Geological Society 137, 773–786.
Bristow, T.F., Kennedy, M.J., Derkowski, A., Droser, M.L., Jiang, G., Creaser, R.A., 2009. Mineralogical constraints on the paleoenvironments of the Ediacaran Doushantuo Formation. Proceedings of the National Academy of Sciences 106, 13190–13195.
Burnett, W.C., 1977. Geochemistry and origin of phosphorite deposits from off Peru and Chile. Geological Society of America Bulletin 88, 813–823.
Cloete, T.E., Oosthuizen, D.J., 2001. The role of extracellular exopolymers in the removal of phosphorus from activated sludge. Water Research 35, 3595–3598.
Condon, D., Zhu, M., Bowring, S., Wang, W., Yang, A., Jin, Y., 2005. U–Pb ages from the Neoproterozoic Doushantuo formation, China. Science 308, 95–98.
Cook, P.J., 1992. Phosphogenesis around the Proterozoic–Phanerozoic transition. Journal of the Geological Society 149, 615–620.
Dahanayake, K., Krumbein, W.E., 1986. Microbial structures in oolitic iron formations. Mineralium Deposita 21, 85–94.
Föllmi, K.B., 1996. The phosphorus cycle, phosphogenesis and marine phosphate-rich deposits. Earth-Science Reviews 40, 55–124.
Heggie, D.T., Skyring, G.W., O Brien, G.W., Reimers, C., Herczeg, A., Moriarty, D., Burnett, W.C., Milnes, A.R., 1990. Organic carbon cycling and modern phosphorite formation on the East Australian continental margin: an overview. Geological Society, Special Publications, London, pp. 87–117.
Horton, A., Ivimey-Cook, H.C., Harrison, R.K., Young, B.R., 1980. Phosphatic öoids in the Upper Lias (Lower Jurassic) of central England. Journal of the Geological Society 137, 731–740.
Jiang, G., Kennedy, M.J., Christie-Blick, N., Wu, H., Zhang, S., 2006. Stratigraphy, sedimentary structures, and textures of the Late Neoproterozoic Doushantuo cap carbonate in South China. Journal of Sedimentary Research 76, 978–995.
Jiang, G., Shi, X., Zhang, S., Wang, Y., Xiao, S., 2011. Stratigraphy and paleogeography of the Ediacaran Doushantuo Formation (ca. 635–551 Ma) in South China. Gondwana Research 19, 831–849.
Jimenez-Lopez, C., Chekroun, K.B., Jroundi, F., Rodríguez-Gallego, M., Arias, J.M., González-Muñoz, M.T., 2011. Myxococcus xanthus colony calcification: a study to better understand the processes involved in the formation of this stromatolite-like structure. In: Reitner, J., Quéric, N., Arp, G. (Eds.), Advances in Stromatolite Geobiology. Springer-Verlag, Berlin, pp. 161–181.
Kastner, M., Siever, R., 1979. Low temperature feldspars in sedimentary rocks. American Journal of Science 279, 435–479.
Kendall, B., Creaser, R.A., Selby, D., 2009. ^{187}Re–^{187}Os Geochronology of Precambrian Organic-rich Sedimentary Rocks, vol. 326. Geological Society, London, Special Publications, pp. 85–107.
Knoll, A.H., Barghoorn, E.S., 1974. Ambient pyrite in Precambrian chert: new evidence and a theory. Proceedings of the National Academy of Sciences 71, 2329–2331.
Knorre, H., Krumbein, W.E., 2000. Bacterial calcification. In: Riding, R., Awramik, S.M. (Eds.), Microbial Sediments. Springer-Verlag, Berlin, pp. 25–31.
Lahfid, A., Beyssac, O., Deville, E., Negro, F., Chopin, C., Goffé, B., 2010. Evolution of the Raman spectrum of carbonaceous material in low-grade metasediments of the Glarus Alps (Switzerland). Terra Nova 22, 354–360.
Lepot, K., Benzerara, K., Philippot, P., 2011. Biogenic versus metamorphic origins of diverse microtubes in 2.7 Gyr old volcanic ashes: Multi-scale investigations. Earth and Planetary Science Letters 312, 37–47.
Lepot, K., Philippot, P., Benzerara, K., Wang, G.Y., 2009. Garnet-filled trails associated with carbonaceous matter mimicking microbial filaments in Archean basalt. Geobiology 7, 393–402.
Liu, P.J., Yin, C.Y., Gao, L.Z., Tang, F., Chen, S.M., 2009. New material of microfossils from the Ediacaran Doushantuo Formation in the Zhangcunping area, Yichang, Hubei Province and its zircon SHRIMP U–Pb age. Chinese Science Bulletin 54, 1058–1064.
Liu, Y., Xue, G., Yu, S., Zhao, F., 2006. Role of extracellular exopolymers on biological phosphorus removal. Journal of Environmental Sciences 18, 670–674.
Liu, Y.Q., Liu, Y., Tay, J.H., 2004. The effects of extracellular polymeric substances on the formation and stability of biogranules. Applied Microbiology and Biotechnology 65, 143–148.
Loaëc, M., Olier, R., Guezennec, J., 1997. Uptake of lead, cadmium and zinc by a novel bacterial exopolysaccharide. Water Research 31, 1171–1179.
Manheim, F.T., Pratt, R.M., McFarlin, P.F., 1980. Composition and origin of phosphorite deposits of the Blake Plateau. In: Bentor, Y.K. (Ed.), Marine Phosphorites—Geochemistry, Occurrence, Genesis. Society of Economic Paleontologists and Mineralogists Special publication, Tulsa, pp. 117–137.
McFadden, K.A., Huang, J., Chu, X., Jiang, G., Kaufman, A.J., Zhou, C., Yuan, X., Xiao, S., 2008. Pulsed oxidation and biological evolution in the Ediacaran Doushantuo Formation. Proceedings of the National Academy of Sciences 105, 3197.
McLoughlin, N., Staudigel, H., Furnes, H., Eickmann, B., Ivarsson, M., 2010. Mechanisms of microtunneling in rock substrates: distinguishing endolithic biosignatures from abiotic microtunnels. Geobiology 8, 245–255.
Mino, T., Van Loosdrecht, M., Heijnen, J.J., 1998. Microbiology and biochemistry of the enhanced biological phosphate removal process. Water Research 32, 3193–3207.
Nathan, Y., Nielsen, H., 1980. Sulfur isotopes in phosphorites. In: Bentor, Y.K. (Ed.), Phosphorites—Geochemistry, Occurrence, Genesis. Society of Economic Paleontologists and Mineralogists Special publication, Tulsa, pp. 73–78.
Nelson, G.J., Pufahl, P.K., Hiatt, E.E., 2010. Paleoceanographic constraints on Precambrian phosphorite accumulation, Baraga Group, Michigan, USA. Sedimentary Geology 226, 9–21.
Obst, M., Wehrli, B., Dittrich, M., 2009. $CaCO_3$ nucleation by cyanobacteria: laboratory evidence for a passive, surface-induced mechanism. Geobiology 7, 324–347.
Oehler, D.Z., Robert, F., Walter, M.R., Sugitani, K., Allwood, A., Meibom, A., Mostefaoui, S., Selo, M., Thomen, A., Gibson, E.K., 2009. NanoSIMS: Insights to biogenicity and syngeneity of Archaean carbonaceous structures. Precambrian Research 173, 70–78.
Oehler, D.Z., Robert, F., Walter, M.R., Sugitani, K., Meibom, A., Mostefaoui, S., Gibson, E.K., 2010. Diversity in the Archean biosphere: new insights from NanoSIMS. Astrobiology 10, 413–424.
Papineau, D., 2010. Global biogeochemical changes at both ends of the Proterozoic: insights from phosphorites. Astrobiology 10, 165–181.
Papineau, D., De Gregorio, B.T., Stroud, R.M., Steele, A., Pecoits, E., Konhauser, K., Wang, J.H., Fogel, M.L., 2010. Ancient graphite in the Eoarchean quartz-pyroxene rocks from Akilia in southern Wes Greenland II: isotopic and chemical compositions and comparison with Paleoproterozoic banded iron formations. Geochimica et Cosmochimica Acta 74, 5884–5905.
Pasteris, J.D., 1989. *In situ* analysis in geological thin-sections by laser Raman microprobe spectroscopy: a cautionary note. Applied Spectroscopy 43, 567–570.
Pufahl, P.K., Grimm, K.A., 2003. Coated phosphate grains: proxy for physical, chemical, and ecological changes in seawater. Geology 31, 801–804.
Rais, P., Louis-Schmid, B., Bernasconi, S.M., Reusser, E., Weissert, H., 2008. Distribution of authigenic albites in a limestone succession of the Helvetic Domain, eastern Switzerland. Swiss Journal of Geosciences 101, 99–106.
Riding, R., 2006. Cyanobacterial calcification, carbon dioxide concentrating mechanisms, and Proterozoic–Cambrian changes in atmospheric composition. Geobiology 4, 299–316.
Riggs, S.R., 1979. Phosphorite sedimentation in Florida; a model phosphogenic system. Economic Geology 74, 285–314.
Sanz-Montero, M.E., Rodriguez-Aranda, J.P., García Del Cura, M.A., 2008. Dolomite–silica stromatolites in Miocene lacustrine deposits from the Duero Basin, Spain: the role of organotemplates in the precipitation of dolomite. Sedimentology 55, 729–750.
Schulz, H.N., Schulz, H.D., 2005. Large sulfur bacteria and the formation of phosphorite. Science 307, 416–418.
Shen, Y., Zhao, R., Chu, X., Lei, J., 1998. The carbon and sulfur isotope signatures in the Precambrian–Cambrian Transition series of the Yangtze Platform. Precambrian Research 89, 77–86.
Sheng, G., Yu, H., Li, X., 2006. Stability of sludge flocs under shear conditions: roles of extracellular polymeric substances (EPS). Biotechnology and Bioengineering 93, 1095–1102.
Shields, G.A., Strauss, H., Howe, S.S., Siegmund, H., 1999. Sulphur isotope compositions of sedimentary phosphorites from the basal Cambrian of China: implications for Neoproterozoic–Cambrian biogeochemical cycling. Journal of the Geological Society 156, 943–955.
Soudry, D., Southgate, P.N., 1989. Ultrastructure of a Middle Cambrian primary nonpelletal phosphorite and its early transformation into phosphate vadoids: Georgina Basin, Australia. Journal of Sedimentary Research 59, 53–64.
Southgate, P.N., 1986. Cambrian phoscrete profiles, coated grains, and microbial processes in phosphogenesis: Georgina Basin, Australia. Journal of Sedimentary Research 56, 429–441.
Spötl, C., Longstaffe, F.J., Ramseyer, K., Rüdinger, B., 1999. Authigenic albite in carbonate rocks—a tracer for deep-burial brine migration? Sedimentology 46, 649–666.
Swett, K., Crowder, R.K., 1982. Primary phosphatic oolites from the Lower Cambrian of Spitsbergen. Journal of Sedimentary Research 52, 587–593.
Tyler, S.A., Barghoorn, E.S., 1963. Ambient pyrite grains in Precambrian cherts. American Journal of Science 261, 424–432.
Wacey, D., Kilburn, M.R., McLoughlin, N., Parnell, J., Brasier, M.D., 2008. Use of NanoSIMS in the search for early life on Earth: ambient inclusion trails in a c. 3400 Ma sandstone. Journal of the Geological Society 165, 43–53.
Wirth, R., 2009. Focused Ion Beam (FIB) combined with SEM and TEM: advanced analytical tools for studies of chemical composition, microstructure and crystal structure in geomaterials on a nanometre scale. Chemical Geology 261, 217–229.

Xiao, S., Zhang, Y., Knoll, A.H., 1998. Three-dimensional preservation of algae and animal embryos in a Neoproterozoic phosphorite. Nature 391, 553–558.

Xiao, S., McFadden, K.A., Peek, S., Kaufman, A.J., Zhou, C., Jiang, G., Hu, J., 2012. Integrated chemostratigraphy of the Doushantuo Formation at the northern Xiaofenghe section (Yangtze Gorges, South China) and its implication for Ediacaran stratigraphic correlation and ocean redox models. Precambrian Research 192–195, 125–141.

Ye, L., Chen, Q., Zhao, D., Chen, Z., Liu, K., 1989. The Phosphorites of China. Science Press, Beijing.

Zega, T.J., Nittler, L.R., Busemann, H., Hoppe, P., Stroud, R.M., 2007. Coordinated isotopic and mineralogic analyses of planetary materials enabled by in situ lift-out with a focused ion beam scanning electron microscope. Meteoritics & Planetary Science 42, 1373–1386.

Zhao, D., 1985. Pelletal phosphorites of the Doushantuo Formation in Sinian Period. Acta Petrologica Sinica 1, 41–51.

Zhao, D., 1989. Microstructures of pisolitic and oolitic phosphorites and their genetic characteristics. Acta Petrologica Sinica 4, 66–75.

Zhu, B., Becker, H., Jiang, S., Pi, D., Fischer-Gödde, M., Yang, J., 2013. Re–Os geochronology of black shales from the Neoproterozoic Doushantuo Formation, Yangtze platform, South China. Precambrian Research 225, 67–76.

Zhu, M., Zhang, J., Yang, A., 2007. Integrated Ediacaran (Sinian) chronostratigraphy of South China. Palaeogeography, Palaeoclimatology, Palaeoecology 254, 7–61.